Atmos. Chem. Phys., 25, 12087–12100, 2025
https://doi.org/10.5194/acp-25-12087-2025

Atmospheric Chemistry and Physics
Open Access
EGU

The effect of amino acids on the Fenton and photo-Fenton reactions in cloud water: unraveling the dual role of glutamic acid

Peng Cheng[1,2], Gilles Mailhot[1,3], Mohamed Sarakha[1], Guillaume Voyard[1], Daniele Scheres Firak[4], Thomas Schaefer[4], Hartmut Herrmann[4], and Marcello Brigante[1]

[1]Institut de Chimie de Clermont-Ferrand, Université Clermont Auvergne, CNRS, 63000 Clermont-Ferrand, France
[2]Department of Environmental Engineering, School of Resources and Environmental Science, Wuhan University, 430079 Wuhan, PR China
[3]Laboratoire de Météorologie Physique (LaMP), Université Clermont Auvergne, CNRS, 63000 Clermont-Ferrand, France
[4]Atmospheric Chemistry Department (ACD), Leibniz Institute for Tropospheric Research (TROPOS), 04318 Leipzig, Germany

Correspondence: Marcello Brigante (marcello.brigante@uca.fr)

Received: 11 April 2025 – Discussion started: 7 May 2025
Revised: 1 July 2025 – Accepted: 9 July 2025 – Published: 7 October 2025

Abstract. In this work, glutamic acid (Glu) was selected as a model amino acid (AA) to investigate its complexation with Fe(III) and Fe(II), focusing on its impact on the Fenton reaction and the photolysis of Fe(III) in the cloud aqueous phase. Glu was found to enhance the rate constant for the reaction of Fe(II)–Glu with H_2O_2 to $1.54 \pm 0.13 \times 10^4\ M^{-1}\ s^{-1}$, which is significantly higher than that of classic Fenton reactions (~ 50–$70\ M^{-1}\ s^{-1}$). In contrast, the photolysis quantum yield of the Fe(III)–Glu complex was determined to be 0.037 under solar-simulated irradiation, largely lower than Fe(III)–hydroxy complexes (0.216). In the overall process (Fenton or Fe(III) photolysis), it was found that $^{\bullet}OH$ formation decreased in the presence of Glu. Additionally, the fate of Glu in the presence of Fe(III) was investigated as well as the oxidation process (driven by $^{\bullet}OH$ and ligand-to-metal charge transfer (LMCT) reaction), which led to the formation of short-chain carboxylic acids and ammonium under simulated solar light. Interestingly, these two processes generated different primary short-chain carboxylic acids, indicating distinct mechanisms. This study provides valuable insights into the role and fate of amino acids in atmospheric chemistry, helping to further understand their impact on atmospheric processes.

1 Introduction

The Earth's atmosphere is a dynamic system in which different phases, including gases, aerosol particles, water droplets, and ice particles, are all engaged in complex chemical interactions that continually modify the atmospheric chemical composition (Bianco et al., 2020; Kanakidou et al., 2018). Among these, the cloud aqueous phase stands out as a critical reactive system, encompassing gaseous, liquid, and solid components. In recent years, intensified research efforts have been centered on unraveling the composition of atmospheric cloud waters, significantly advancing our comprehension of multiphase chemistry within the atmosphere (Bianco et al., 2018). Common components identified in both aerosols and cloud water include inorganic ions, transition metal ions (TMIs) such as iron (Angle et al., 2021; Bianco et al., 2017), and organic carbon (Battaglia et al., 2019), notably amino acids (AAs). However, the influence of AAs on iron redox chemistry and hydroxyl radical ($^{\bullet}OH$) production in cloud water remains insufficiently understood.

Recent investigations have unveiled the presence of reactive oxygen species (ROS) in viscous aerosol particles, high-

lighting their pronounced reactivity in such environments (Alpert et al., 2021; Edwards et al., 2022). Hydroxy radicals ($^{\bullet}OH$) emerge as primary ROS in the atmospheric water phase, with concentrations estimated between 10^{-14} and $10^{-12}\,M^{-1}$ (Bianco et al., 2020; Gligorovski et al., 2015). Key sources of $^{\bullet}OH$ include gas–droplet partitioning and in situ formation through processes like photolysis at surfaces or in the bulk phase, such as the photolysis of TMI and hydrogen peroxide (H_2O_2) (Bianco et al., 2015; Tilgner et al., 2013).

Iron (Fe), copper (Cu), and manganese (Mn) have gained prominence as pivotal metals in atmospheric chemical processes due to their elevated concentrations, with Fe averaging around $10^{-6}\,M$ in the atmospheric aqueous phase (Sorooshian et al., 2013). Experimental evidence and literature emphasize the crucial role of iron, particularly via (photo-)Fenton and (photo-)Fenton-like processes, in the generation and budgeting of $^{\bullet}OH$ (Reactions R1–R5) (Guo et al., 2014; Tilgner et al., 2013).

$$[Fe(H_2O)_6]^{3+} \xrightarrow{h\nu} [Fe(H_2O)_5]^{2+} + H^+ + {}^{\bullet}OH \quad (R1)$$

$$[Fe(H_2O)_5OH]^{2+} \xrightarrow{h\nu} [Fe(H_2O)_5]^{2+} + {}^{\bullet}OH \quad (R2)$$

$$[Fe(H_2O)_5]^{2+} + H_2O_2 \longrightarrow [Fe(H_2O)_5OH]^{2+} + {}^{\bullet}OH \quad (R3)$$

$$[Fe(H_2O)_6]^{3+} + H_2O_2 \longrightarrow [Fe(H_2O)_5]^{2+} + HO_2^{\bullet} + H_2O + H^+ \quad (R4)$$

$$[Fe(H_2O)_5OH]^{2+} + H_2O_2 \longrightarrow [Fe(H_2O)_5]^{2+} + HO_2^{\bullet} + H_2O \quad (R5)$$

While Fe(III)/Fe(II) ions precipitate as oxides or hydroxides at pH higher than 4.0, in the cloud water phase, iron complexes with organic ligands enhance stability under typical cloud water photooxidation conditions (Soriano-Molina et al., 2018; Yuan et al., 2020). Various organic ligands, including carboxylic acids and aldehydes, have been extensively studied (Long et al., 2013; Marion et al., 2018; Soriano-Molina et al., 2018). However, less than 30 % of the dissolved organic carbon (DOC) in the cloud aqueous phase has been molecularly characterized, with AAs constituting a significant portion of DOC (Bianco et al., 2016). Numerous field studies have confirmed the presence of AAs in cloud water, rain, fog, and aerosols, with concentrations typically ranging from low nanomolar to micromolar levels, depending on the location and sampling method (Matos et al., 2016; van Pinxteren et al., 2023; Renard et al., 2022; Triesch et al., 2021). For example, Renard et al. (2022) detected more than 15 AAs in cloud water collected at Puy de Dôme, France, with glutamate being one of the most abundant species. These compounds originate from both primary emissions (e.g., bioaerosols, ocean spray) and secondary atmospheric processes (e.g., processing of proteins or peptides within clouds) (Mace et al., 2003; Samy et al., 2011). Amino acids, as key nitrogen-containing components in organic matter, can significantly affect the oxidation capacity of cloud water through free radical scavenging and metal complexation reactions (Bianco et al., 2016; Marion et al., 2018), but their specific atmospheric reactivity and transformation mechanisms are still unclear. The photochemical behavior and fate of AAs in the atmosphere remain relatively unexplored. For example, tryptophan can undergo direct photolysis, producing low-molecular-weight compounds and dimerization products under solar-simulated conditions. Recent investigations into the fate of the Fe(III)–aspartate complex demonstrate ligand-to-metal charge transfer reactions (LMCT) and the formation of ammonia and short-chain carboxylic acids (Marion et al., 2018).

However, the effect of the complexation between Fe(II) and AAs on the rate of Fenton reaction and the yield of $^{\bullet}OH$ in the atmosphere has not yet been investigated. Moreover, the effect of the complexation between Fe(III) and AAs on the quantum yield of atmospheric photolysis of Fe(III) deserves further investigation, since both processes highly affect the budget of $^{\bullet}OH$ during the day and night in the atmosphere. In addition, the complexation between Fe(III) and AAs introduces two distinct photooxidation pathways: the photolysis of iron–amino acid (Fe-AA) complexes and reactions between AAs and (photo)-generated $^{\bullet}OH$. Although both pathways significantly contribute to the transformation of AAs in cloud water and impact inorganic and organic chemical compositions, their mechanisms still lack further study, especially in terms of products generation.

This study specifically focuses on glutamic acid (Glu), an AA regularly detected in cloud water and aerosols (van Pinxteren et al., 2012; Triesch et al., 2021), and on the investigation of its impact on iron (Fe(II)/Fe(III)) reactivity. The study explored (i) the effect of Glu on the rate and $^{\bullet}OH$ yield of the Fenton reaction and (ii) the effect of Glu on the $^{\bullet}OH$ production and Fe(II) quantum yield during the Fe(III) photolysis. In addition, the study explores (iii) two pathways of Fe(III) and Fe(III)–Glu complex photolysis: the LMCT process and the reaction between Glu and $^{\bullet}OH$, assessing their respective contributions to the fate of Glu. Utilizing competitive kinetic experiments, the contributions of each pathway were estimated, and a detailed investigation of the formation and chemical mechanisms of transformation products was carried out. Ultimately, our study aims to quantify the diverse contributions of different pathways in amino acid conversion in the presence of iron.

2 Material and methods

2.1 Chemicals

All chemicals were used without further purification: Fe(III) perchlorate (99.9 %), Fe(II) perchlorate (99.9 %), L-glutamic acid monosodium salt (Glu, 99 %), hydrogen peroxide (H_2O_2, 30 %), malonic acid (99.0 %), and 2,4-dinitrophenylhydrazine (DNPH, 97 %) were purchased from Sigma Aldrich. Sodium formate (99.0 %), potassium oxalate

monohydrate (99.0 %), sodium succinate dibasic (98.0 %), and 3-(2-pyridyl)-5,6-diphenyl-1,2,4-triazine-p, p′-sulfonic acid monosodium salt hydrate (ferrozine, 97 %) were purchased from Fluka. Ammonium acetate (99.3 %) was purchased from Fisher. Water was purified using a reverse osmosis RIOS 5 and Synergy (Millipore) device (resistivity 18.2 MΩ cm, DOC < 0.1 mg L^{-1}). All solutions were prepared in Milli-Q water.

2.2 Experimental procedure

2.2.1 Fenton reaction

The Fenton experiments were carried out with Fe(II) perchlorate at room temperature and a pH of 5.6 ± 0.1 (kinetic experiments) and 3.8 ± 0.1 (electron spin resonance (ESR) experiments). The pH of 5.6 was chosen to favor the formation of Fe(II)–Glu complexes during the kinetic studies, while the lower pH of 3.8 was selected for ESR experiments, as $^{\bullet}$OH detection by ESR is more effective under acidic conditions. These two pH values fall within the typical range observed in atmospheric cloud water. Specifically, pH of 3.8 represents more acidic conditions often found in polluted regions, whereas pH of 5.6 reflects the composition of cloud water in remote or less impacted environments (Pye et al., 2020; Shah et al., 2020). This range enables the assessment of the system's behavior under environmentally relevant conditions.

The Fenton kinetic experiments were initiated by the addition of the H_2O_2 stock solution. Hence, the designed H_2O_2 concentrations are 100 and 25 µM in kinetics and ESR experiments respectively. The solution was continuously stirred during the reaction. The pH of the solution was adjusted using $HClO_4$ or NaOH solutions. The samples were taken every 15 s and mixed with a solution of ferrozine in phosphate buffer (pH $= 7.0 \pm 0.1$) (Gabet et al., 2023). Phenol was used as a $^{\bullet}$OH scavenger in the experiment. As a scavenger, the required concentration of phenol was calculated to quench $^{\bullet}$OH so that theoretically 99 % of $^{\bullet}$OH can be trapped via reacting with phenol. The same method was used in the presence of glutamic acid (Glu) to study the Fe(II)–Glu complex Fenton-like reaction at the same pH. To get different fractions of Fe(II)–Glu, Fe(II) was mixed with varying concentrations of Glu solution (0–25 mM) to calculate the rate constant of the Fenton reaction. The experimental data were analyzed using Origin 2019 software. To determine and quantify the $^{\bullet}$OH generation in the Fenton reaction, the ESR experiment was carried out using 5,5-dimethyl-1-pyrroline-N-oxide (DMPO) as the spin trap. $Fe(ClO_4)_2$ and H_2O_2 were mixed with DMPO at a pH of 3.8 ± 0.1. The pH was set because the ESR signal intensity was lower at a higher pH $= 4.0$. ESR spectroscopy was performed on a Bruker EMX-plus spectrometer using the resonator 4119HS. Detailed information (kinetics data processing method and ESR experiment) was provided in the Supplement (Sect. S1).

2.2.2 Photolysis of Fe(III)

To study the Fe(III) photolysis, isopropanol was used as a scavenger in the solution to quench the generated $^{\bullet}$OH radicals. The pH of the solution was adjusted to 3.8 ± 0.1 with $HClO_4$ or NaOH solutions. The Fe(III) solution was irradiated in a Pyrex jacked cylindrical reactor (Fig. S1 in the Supplement) with a circulation cooling system to keep a constant temperature of 283 ± 0.2 K. The reactor was located at the focal point of a 500 W xenon lamp equipped with a Pyrex filter to remove wavelengths < 290 nm and a water filter for infrared radiation absorption. The solution was stirred with a Teflon-coated magnetic stirring bar to ensure homogeneity. The same setup was used for the photolysis experiments in the presence of Fe(III)–Glu complexes. Different fractions of Fe(III)–Glu were achieved by adding different amounts of a Glu 50 mM stock solution (designed [Glu] = 0–200 µM).

The emission spectrum of the irradiation setup was recorded using a calibrated CCD camera (Ocean Optics USB 2000 + UV–Vis) coupled with an optical fiber. An irradiance of 8.38×10^3 µW cm^{-2} was determined between 290 and 500 nm as shown in Fig. S2. Compared to the natural solar emission spectrum, the UV region between 290 and 400 nm, which has a role in driving the photoreaction of Fe(III) and Fe(III)–Glu, shows quite a similar spectral profile, as reported in our previous publication (Bianco et al., 2015). The energy and photonic flux (I_0) of the polychromatic irradiation at every nanometer wavelength are listed in Table S1. Detailed information about the calculation of the Fe(III) and Fe(III)–Glu photolysis quantum yield is given in the Supplement (Sect. S2.1 and S2.2). To quantify the $^{\bullet}$OH generation during the Fe(III) photolysis, isopropanol was used in excess (10 mM) as a selective $^{\bullet}$OH probe. Isopropanol reacts with $^{\bullet}$OH to form acetone, which was quantified by high-performance liquid chromatography (HPLC; see Sect. 2.3) (Motohashi and Saito, 1993).

2.2.3 Photodegradation of Glu

To investigate the fate of Glu in various systems, experiments were performed using the previously described photoreactor setup. Glu solutions, either alone or mixed with Fe(III) and/or H_2O_2, were irradiated under simulated solar light at pH 3.8 ± 0.1. Samples were collected at specific time intervals and analyzed using HPLC-MS. To calculate and compare the photodegradation kinetics of Glu in different systems, a pseudo-first-order kinetic model was applied, expressed as Eq. (1):

$$-\ln(C_t/C) = k_{\mathrm{obs}} t, \tag{1}$$

where C_0 represents the initial concentration of Glu, and C_t is the concentration of Glu at time t of irradiation. In addition, IC-MS and total organic carbon (TOC) analyses were performed to identify the generated by-products and assess the mineralization of Glu (see Sect. 5.3).

2.3 Study of the speciation of the Fe(III)/Fe(II)–Glu complex

The speciation of the Fe(III)/Fe(II)–Glu complex was studied using the Hyss 2009 software. This analysis included the iron, iron–aqua, iron–hydroxy, and iron–Glu complexes in the solution. The parameters used in the software, such as iron and Glu concentrations, kept consistent with the one in the experimental procedure. The stability constants ($\log K$) used for the complexes, such as the Fe(II)–Glu and Fe(III)–Glu complexes, are listed in Table S2. These constants are derived from the Visual MINTEQ database or NIST database 46 and have been corrected for a temperature of 25 °C and an ionic strength (I) of 0 M. The detailed method is provided in the Supplement (Sect. S3).

2.4 Chemical analysis

2.4.1 Fe(II), H_2O_2, and acetone quantification

Iron (II) concentration was determined using ferrozine, which forms a stable magenta complex with Fe(II) (Fe(II) ferrozine) (Gabet et al., 2023). Hydrogen peroxide concentration during experiments was determined by using a spectrofluorometric quantification method (Bader et al., 1988). The concentration of generated acetone in the solution was evaluated by HPLC (Shimadzu NEXERA XR HPL) equipped with a photodiode array detector and an autosampler (Wang et al., 2005). Figure S3 shows the calibration curve of Fe(II), H_2O_2, and acetone. More details are given in the Supplement (Sect. S4).

2.4.2 UPLC-MS, IC-MS, and TOC

The quantification of glutamic acid (Glu) and the identification of its transformation products were conducted using a Thermo Scientific Orbitrap Q-Exactive high-resolution mass spectrometer (HRMS) coupled with a Thermo Scientific Ultimate 3000 RSLC ultra-high-performance liquid chromatography (UPLC) system. The quantification of carboxylic acid by-products and NH_4^+ resulting from Glu degradation was performed using a Thermo Fisher Scientific ICS-6000 Ionic chromatograph interfaced with a simple quadrupole mass spectrometer (ISQ-EC-Thermo Scientific). The total organic carbon (TOC) concentration in the aqueous solution was followed by a Shimadzu TOC 5050A analyzer. Detailed information is reported in the Supplement (Sect. S5).

2.5 Kinetic modeling

To verify the obtained experimental rate constants of the reaction between Fe(II)–Glu and H_2O_2, COPASI software was utilized to simulate the kinetics of Fe(II) consumption and generation of OH in the Fenton reaction in the presence of Glu using the default settings of the deterministic LSODA algorithm to solve ordinary differential equations (Hoops et al., 2006). The chemical reactions considered in the model are provided in Table S3. The majority of rate constants used in the model were available in the literature or obtained from experimental results. For the unknown or uncertain rate constants, the value is obtained from the estimation according to a similar reaction.

3 Results and discussion

To investigate the effect of Glu on the Fe(II)/Fe(III) cycle, a complex set of experiments was performed. First, the complexation of Fe(II)/Fe(III) with Glu was studied as a function of pH and the initial concentration of Glu. Second, to study the effect of Glu on the Fenton reaction, its rate constants and $^{\bullet}OH$ generation in the presence of Glu were obtained experimentally and using the kinetic model. The formation rates of Fe(II) and $^{\bullet}OH$ were determined from Fe(III) photolysis with or without Glu. Finally, the mechanism of Glu phototransformation was reported.

3.1 Complexation of Glu with Fe(II)/Fe(III)

The Fe speciation was initially investigated to understand how Glu interacts with iron ions under various conditions with Hyss2009 software. Figure S4a shows the speciation of 20 µM Fe(II) in the presence of Glu (0.2–25 mM) across a pH range of 4 to 10. It can be observed that Fe(II) predominates until pH = 5, while the fraction of the Fe(II)–Glu complex increases after this pH. Hence, a higher pH (5.6) was selected for the Fenton reaction to guarantee the presence of complex, while still working under aerosol/cloud conditions and to avoid iron precipitation occurring at higher pH values. At pH 5.6, the Fe(II)–Glu complex accounts for 2.2 % in the presence of 20 µM Fe(II) and 25 mM Glu. The complex fractions at varying Glu concentrations at pH = 5.6 are provided in Table S4.

Figure S4b shows the simulated speciation of Fe(III) (100 µM) as a function of pH in the presence of Glu (10–20 µM). The Fe(III)–aqua, Fe(III)–hydroxy, and Fe(III)–Glu complexes were observed as a function of the pH. At pH = 3.8, [Fe(III)] = [Glu] = 100 µM, the Fe(III)–hydroxy complexes $Fe(OH)^{2+}$ and $Fe(OH)_2^+$ represent 24.4 % and 22.8 % of the total Fe(III) concentration respectively. In contrast, the Fe(III)–Glu complex accounts for 52.3 % of the total Fe(III), while the Fe(III)–aqua complex constitutes only 0.5 %. The UV–Vis spectra of Fe(III), Glu, and Fe(III)–Glu complex are depicted in Fig. S2. The characteristic absorption band of Fe(III) with a maximum at 297 nm, corresponding to the charge transfer bands of $Fe(OH)^{2+}$, becomes attenuated in the presence of Glu. Moreover, the UV–Vis spectrum of the Fe(III)–Glu mixture differs from that of Fe(III) and Glu alone or the simple overlap of their individual spectra, confirming the formation of a stable Fe(III)–Glu complex (Samavat et al., 2007). The fractions of the gen-

erated complex in the presence of different Glu concentrations at pH = 3.8 are given in Table S5. For the sake of simplicity, Fe(III)/Fe(II)–hydroxy and Fe(III)/Fe(II)–aqua complexes are hereafter referred as Fe(III) and Fe(II).

3.2 Fenton reaction process in the presence of Glu

3.2.1 Fe(II) oxidation

To study the effect of Glu on the kinetics of the Fenton reaction and determine the rate constant of the reaction of Fe(II)–Glu with H_2O_2, experiments were performed using different concentrations of Glu. Figure 1a shows the faster Fe(II) concentration decreases when the Glu concentration increases, which indicates that Glu can increase the reaction rate of Fe(II) with H_2O_2. This is likely due to the formation of the Fe(II)–Glu complex, which has a high reaction rate constant with H_2O_2. As seen in Fig. 1b, the data obtained by plotting $\frac{-\frac{d[Fe(II)]}{dt}}{[H_2O_2][Fe(II)]}$ as a function of the fraction of Fe(II)–Glu can be fitted with a linear equation $y = ax + b$, where a is equal to $1.54 \pm 0.13 \times 10^4\ M^{-1}\ s^{-1}$ and represents the rate constant of reaction of Fe(II)–Glu with H_2O_2, and b is equal to rate constant of Fe(II) with H_2O_2 $\left(-\frac{d[Fe(II)]}{dt}\right.$ data are provided in Table S4$\left.\right)$. Notably, the obtained rate constant is much higher than the rate constant of the classic Fenton reaction, which has a rate constant of about 50–70 $M^{-1}\ s^{-1}$ (Kremer, 2003; Neyens and Baeyens, 2003; Rachmilovich-Calis et al., 2009). Moreover, the value is about 5 times higher than our recently reported value for the reaction between Fe(II)-oxalate and H_2O_2 ($3.2 \pm 0.3 \times 10^3\ M^{-1}\ s^{-1}$) (Scheres Firak et al., 2025). Despite the quantitative difference, both of the obtained values are of the same order, highlighting the significant reactivity enhancement conferred by organic ligand coordination. The reason behind this increase is likely due to the Fe(II)–Glu complex accessing a lower reduction potential calculated to be +0.241 V compared with the Fe(II) (+0.771 V) (Strathmann and Stone, 2002), which contributes to the higher rate constant of the reaction of Fe(II)–Glu with H_2O_2.

Then the Fenton reaction model was used to fit the experimental data to verify the rate constant value of the reaction between Fe(II)–Glu and H_2O_2. As shown in Fig. 1a, the experimental data of Fe(II) kinetics can be well fitted by the model. The fitted rate constant value of the reaction between Fe(II)–Glu and H_2O_2 was obtained at a range of 1.2×10^4 to $1.8 \times 10^4\ M^{-1}\ s^{-1}$, which is very close to the experimental results.

3.2.2 $^{\bullet}$OH quantification

To study the effect of Glu on the $^{\bullet}$OH generation, EPR experiments were carried out. Figure 1c shows the EPR signal of DMPO-OH (1 : 2 : 2 : 1) increases with the reaction time, indicating that $^{\bullet}$OH is continuously generated. In Fig. 1d, the concentration of generated $^{\bullet}$OH decreases when the Glu concentration increases from 0 to 1.0 mM. This trend suggests no direct $^{\bullet}$OH generation occurs from the reaction of Fe(II)–Glu with H_2O_2. This hypothesis has been verified by employing a kinetic model. The experimental data can be well fitted using the experimental rate constant $k_{Fe(II)-Glu/H_2O_2} = 1.54 \pm 0.13 \times 10^4\ M^{-1}\ s^{-1}$.

3.3 Fe(III) photolysis in the presence of Glu

3.3.1 Fe(II) formation

To study the effect of Glu on the kinetics and determine the quantum yield of the photolysis of Fe(III), the photo-driven reaction was carried out in the presence of different concentrations of Glu (0–200 µM) under simulated solar light. Figure S5a shows that the Fe(II) generation rate decreases when the Glu concentration increases, which indicates that Glu slightly reduces the photoactivity of Fe(III). As shown in Fig. 2a, plotting the apparent quantum yield of Fe(II), $\Phi^{obs}_{Fe(II)}$, as a function of the fraction of Fe(III)–Glu complex, the quantum yield of Fe(II) decreases with the fraction of Fe(III)–Glu complex increasing. The linear fit can depict the kinetic data well, with a regression coefficient equal to 0.99. As mentioned in S2, the intercept represents the Fe(II) quantum yield of Fe(III) photolysis under polychromatic irradiation, which is equal to 0.216 ± 0.004. This result is consistent with previous data (Bossmann et al., 1998). The slope represents the difference between Fe(II) quantum yield of the Fe(III) photolysis and the value of the photolysis of Fe(III)–Glu complex $\left(\Phi^{Fe(II)}_{Fe(III)--Glu} - \Phi^{Fe(II)}_{Fe(III)}\right)$, which is equal to −0.179; hence the Fe(II) quantum yield during the photolysis of Fe(III)–Glu is calculated to be 0.037 ± 0.004. Weller et al. (2013) investigated the photolysis of Fe(III)–carboxylate complexes and found the quantum yield of Fe(II) formation from Fe(III)–malonate at 308 and 351 nm, with values of 0.024 ± 0.001 and 0.040 ± 0.003 respectively. This suggests that Fe(III) complexes containing unsubstituted carboxylates as a functional group exhibit lower quantum yields compared to Fe(III).

3.3.2 $^{\bullet}$OH generation

Since the photolysis of Fe(III) is an important process affecting the budget of $^{\bullet}$OH in the atmosphere (Guo et al., 2014), the effect of Glu on the $^{\bullet}$OH produced by the photolysis process of Fe(III) was investigated. As shown in Fig. S5b, the acetone generation rate decreases when the Glu concentration increases, indicating that the $^{\bullet}$OH generation of the Fe(III) photolysis decreases in the presence of Glu (Fig. 2b). The most likely reason for this observation is the decrease in the Fe(III) hydroxy complexes (Table S5); hence the decrease in the $^{\bullet}$OH yield as the Fe(III)–Glu does not produce $^{\bullet}$OH directly but instead forms Glu oxidation products (Glu_{ox}) through the LMCT process. These Glu oxidation products can complex Fe(II) and regenerate Fe(III), a mech-

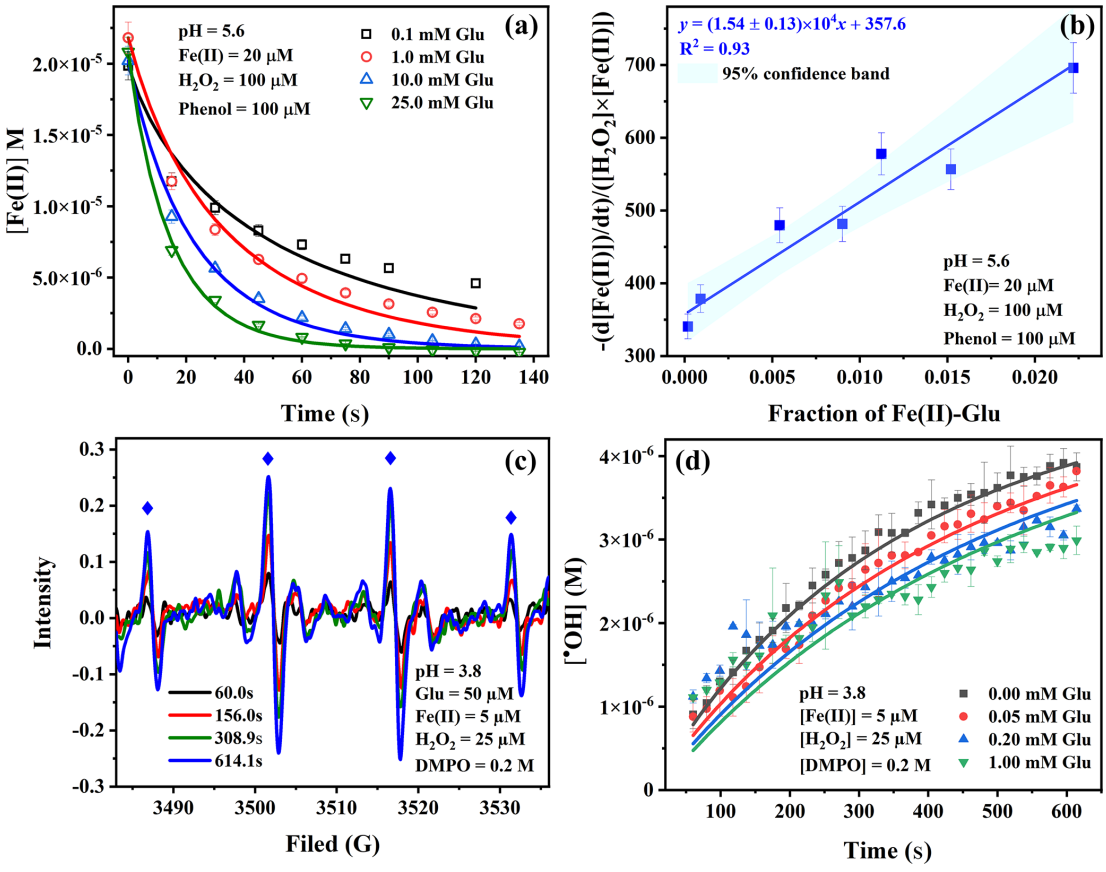

Figure 1. Effect of different concentrations of Glu on the kinetics of Fenton reaction **(a)**, apparent rate constant as a function of the fraction of Fe(II)–Glu **(b)**, signal of EPR corresponding to DMPO-OH (the blue diamond marks the position of the characteristic 1 : 2 : 2 : 1 EPR signal of the DMPO-OH adduct) **(c)**, and the kinetics of •OH generation in Fenton reaction in the presence of different concentrations of Glu **(d)**. Points are determined experimentally, and lines in panels **(a)** and **(d)** are the fit of data using the kinetic model.

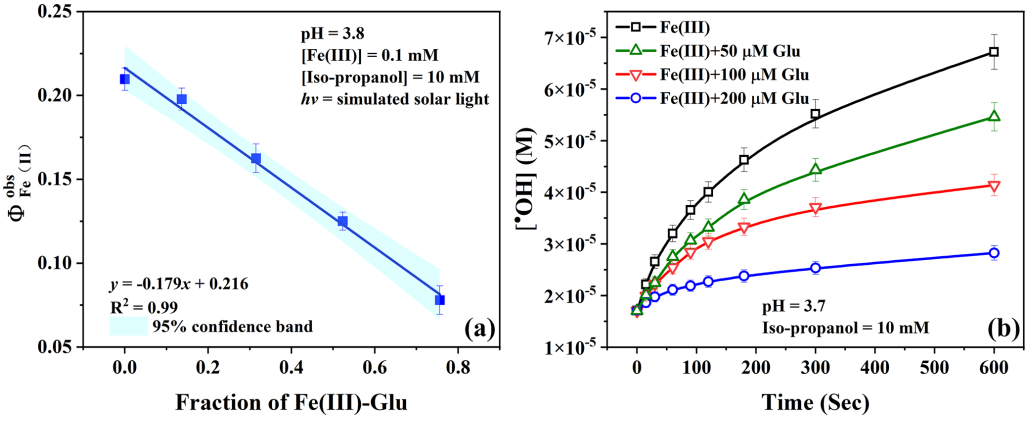

Figure 2. **(a)** The quantum yield of Fe(III) photolysis as a function of the fraction of Fe(III)–Glu complex and **(b)** the •OH generation of Fe(III) photolysis in the presence of different concentrations of Glu. The continuous lines are visual guides generated by applying the "Connect B-Spline" function in Origin 2019.

anism known as "the quenching mechanism" proposed by Wang et al. (2010). This process reduces the apparent quantum yield of Fe(II) to 0.037 ± 0.004. This result illustrates that $^{\bullet}OH$ generation could be less in the presence of amino acids during the daytime in the atmosphere.

3.4 The fate of Glu in the presence of Fe(III) under simulated solar light

3.4.1 Photodegradation of glutamic acid in different systems

All the above results indicate that Glu not only stabilizes Fe(III)/Fe(II) at higher pH but also influences the Fenton reaction and photolysis of Fe(III) processes. The main effects were that the complexes altered the individual reaction rate constants and $^{\bullet}OH$ production. On the other hand, Glu as the organic ligand can also be degraded during the reaction, especially photo-reaction in the atmosphere. Figure 3 shows the photodegradation kinetics of Glu in different systems, and the first-order fitted data are reported in Fig. S6. As expected, when only Glu was present in the solution, no significant degradation ($k_{obs} = 1.90 \pm 0.22 \times 10^{-5}\ s^{-1}$) was observed after 1 h of irradiation, as shown in the UV–Vis spectrum (Fig. S2) of Glu, since there is no significant light absorption in the solar spectrum. The Glu degradation slightly increased in the presence of 1 mM H_2O_2 with a degradation constant of $2.44 \pm 0.45 \times 10^{-5}\ s^{-1}$ corresponding with a degradation of 8.5 % in 1 h, which is due to the formation of $^{\bullet}OH$ radicals via the photolysis of H_2O_2. In addition, the rate constant of $^{\bullet}OH$ with Glu is $2.3 \times 10^8\ M^{-1}\ s^{-1}$ (Masuda et al., 1973), which means that the reaction between those two components is one of the most important processes for the degradation of Glu. Considering the second reaction rate constant between $^{\bullet}OH$ and H_2O_2 ($k^{\bullet OH}_{H_2O_2} = 2.7 \times 10^7\ M^{-1}\ s^{-1}$) (Christensen et al., 1982), it can be argued that under adopted conditions, about 55 % of generated $^{\bullet}OH$ was quenched by the H_2O_2, which led to the formation of less reactive hydroperoxyl radical/superoxide anion pair ($HO_2^{\bullet}$ / $O_2^{\bullet-}$).

Moreover, in the presence of Fe(III), the mixture of Fe(III)–hydroxy and Fe(III)–Glu complexes underwent the photolysis process. As shown in Fig. 3a, about 85 % of Glu was degraded with a first-order rate constant of $4.99 \pm 0.24 \times 10^{-4}\ s^{-1}$ after 1 h of irradiation. This high efficiency is likely due to two different Glu degradation pathways: one is due to the reaction between Glu and the $^{\bullet}OH$ radicals generated by photolysis of Fe(III) (Reaction R1 and R2), and the other one is due to the direct photolysis of Fe(III)–Glu leading to the formation of Fe(II) and oxidation products of the organic ligand (Glu_{ox}). The synergistic effect of those two processes highly improved the Glu degradation efficiency. To distinguish between the contributions of the two degradation pathways, methanol was selected as a $^{\bullet}OH$ scavenger ($k^{\bullet OH}_{Methanol} = 9.7 \times 10^8\ M^{-1}\ s^{-1}$) (Buxton et al., 1988). As illustrated in Fig. 3b, Glu degradation was inhibited by 60 %, indicating that 40 % of Glu degradation originates from the photolysis of Fe(III)–Glu complexes. Interestingly, this ratio aligns with the proportion of Fe(III) and Fe(III)–Glu complexes in the system (Table S5), confirming the aforementioned conclusion. Furthermore, the degradation of Glu resulting from the photolysis of Fe(III)–Glu complexes likely does not involve a $^{\bullet}OH$ process (Sun et al., 1998; Weller et al., 2013).

Glu degradation was observed to be approximately 100 % after 20 min of irradiation in the presence of Fe(III) and H_2O_2, with a first-order rate constant of $5.13 \pm 1.03 \times 10^{-3}\ s^{-1}$. Compared to conditions with only Fe(III) or H_2O_2, the efficiency of Glu degradation significantly improves due to the photo-Fenton reaction in the system, which greatly accelerates the formation rate of reactive species and consequently enhances the degradation rate of Glu.

3.4.2 Analysis of photodegradation products of glutamic acid

To distinguish the Glu degradation processes resulting from the photolysis of Fe(III)–Glu complexes and from those caused by $^{\bullet}OH$ attack, which might lead to the formation of different products, a series of experiments were conducted. In all cases, IC-MS was employed to analyze the formation of short-chain carboxylic acid and ammonium ions, providing a deeper understanding of the photochemical reaction products in various systems under simulated solar light.

Figure 4a depicts the formation of ammonium (NH_4^+) in different systems under irradiation. A positive correlation is observed between the rate of NH_4^+ production and the rate of Glu degradation in various systems, suggesting the occurrence of deamination during the Glu degradation. Additionally, several carboxylic acids (i.e., acetic, formic, succinic, malonic, and oxalic acids) were detected (Table S6), as illustrated in Fig. 4b, c, and d. Notably, the concentration of generated carboxyl acids is considerably lower than that of NH_4^+.

After 120 min of irradiation, low concentrations of generated NH_4^+ and carboxylic acid were determined during Glu photolysis due to small Glu degradation (see Figs. 4a and S7). In the presence of 1 mM H_2O_2, NH_4^+ concentration increased to 7.8 µM within 120 min, representing a 3-fold increase compared to that produced during Glu photolysis. Figure 4b demonstrates the formation of carboxylic acids with formate and succinate as primary carboxylate products, while a negligible concentration of acetate (less than 1 µM) was also detected, all of which are products of $^{\bullet}OH$ attack.

In the presence of Fe(III), NH_4^+ concentration increased to 69.5 µM (Fig. 4a) within 60 min. Simultaneously, the generation of carboxyl acids, such as formate, acetate, and oxalate was observed. The concentration of formate initially increased, reaching a maximum value of 8.7 µM at

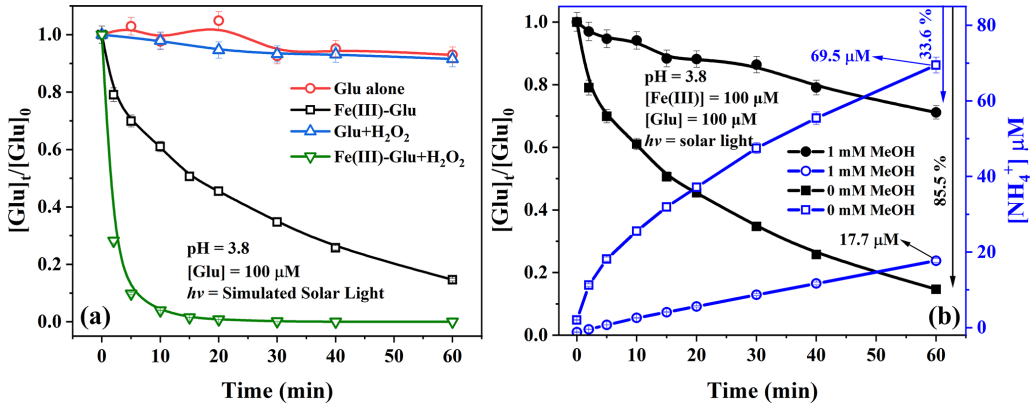

Figure 3. **(a)** Photodegradation of Glu in different systems: Glu alone, Fe(III)–Glu, Glu + H_2O_2, and Fe(III)–Glu + H_2O_2 ([Glu] = 100 µM, [Fe(III)] = 100 µM, [H_2O_2] = 1 mM). **(b)** Photodegradation of Glu and ammonium generation in the Fe(III)–Glu system in the absence and presence of MeOH. The continuous lines are visual guides generated by applying the "Connect B-Spline" function in Origin 2019.

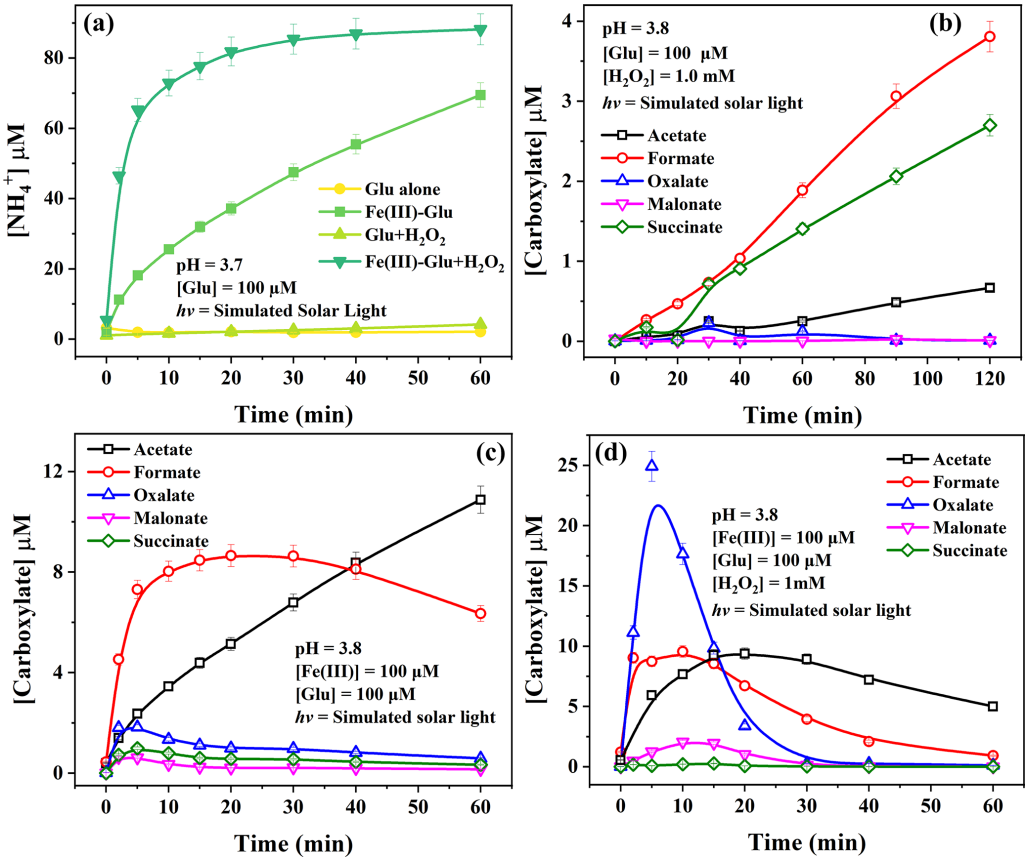

Figure 4. The by-products of Glu degradation under solar light **(a)** formation of NH_4^+ in different systems and formation of carboxylic acids **(b)** in the system Glu + H_2O_2, **(c)** in the system Glu + Fe(III), and **(d)** in the system Glu + Fe(III) + H_2O_2. The continuous lines are visual guides generated by applying the "Connect B-Spline" function in Origin 2019.

20 min, followed by a decline to about 6.4 µM at 60 min. The reason for the decline is probably due to the reaction of formate with photo-generated $^{\bullet}OH$ ($k^{\bullet OH}_{Formate} = 1.3–1.4 \times 10^8\ M^{-1}\ s^{-1}$) (Buxton et al., 1988). Acetate concentration steadily increased throughout the reaction, reaching 10.9 µM at 60 min. Other carboxylates, such as succinate, malonate, and oxalate, were found in lower concentration, with a maximum of around 2 µM within 5 min. As mentioned above, in the presence of Fe(III), the Glu degradation can be attributed to two pathways: one resulting from $^{\bullet}OH$ attack

and the other from the photolysis of the Fe(III)–Glu complexes.

To distinguish the contribution of these two pathways, isopropanol was employed to quench $^{\bullet}OH$ in solution generating acetone as the main product (Motohashi and Saito, 1993). As shown in Fig. S8, only acetate and formate were generated (succinate, malonate, and oxalate were not detected). Moreover, the presence of isopropanol significantly enhanced the formation of acetate compared to values observed with only Fe(III) and Glu. This is likely due to the H-donor effect of the added alcohol or to the reaction between acetic acid radicals ($HOOCCH_2^{\bullet}$) and $HO_2^{\bullet}$ radicals, the latter being generated through the reaction of $^{\bullet}OH$ with the alcohol. As shown in Fig. S8, the concentration of generated formate in the presence of isopropanol and Fe(III) is lower than that when only Fe(III) is added, suggesting that formate was likely not a primary product generated from the photolysis of Fe(III)–Glu complexes but rather may be produced by $^{\bullet}OH$ attack of other carboxylic acids. For example, the generated acetate can be further oxidized reacting with $^{\bullet}OH$ leading to the formation of formate.

This finding is consistent with the result observed in the presence of H_2O_2 alone (Fig. S7). In the presence of $^{\bullet}OH$ scavenger, the generation of NH_4^+ was strongly inhibited with the formation of 17.7 µM instead of 69.5 µM after 1 h (as previously reported in Fig. 3b), which indicates that the NH_4^+ formation is mainly due to the $^{\bullet}OH$ attack process. Furthermore, a significant NH_4^+ (up to 69.5 µM within 60 min) can be observed in the presence of both Fe(III) and H_2O_2 (Fig. 4d). Oxalate, acetate, and formate were observed as the predominant carboxylate products with higher concentrations, reaching 24.9, 9.4, and 9.6 µM respectively, before decreasing. Additionally, the formations of malonate (2.1 µM) and succinate (0.3 µM) were observed at lower concentrations during the photoreaction. In the presence of H_2O_2 and Fe(III), the Fe(III)/Fe(II) cycle is enhanced via the photo-Fenton reaction. Fe(II) is rapidly re-oxidized to Fe(III) to produce $^{\bullet}OH$, which then directly attacks Glu, leading to degradation. Fe(III) is re-complexed by Glu, reactivating the photoreaction and then the iron cycle. Therefore, the addition of H_2O_2 favors deamination as well as various carbon-centered radical combination interactions. The rapid depletion of oxalate after 30 min implies that photolysis of complexes between Fe(III) and polycarboxylic acid also occurs in this system, while formate, acetate, and malonate exhibit similar tendencies with different reaction rates. To verify the mineralization of Glu during the reaction, TOC was followed. As shown in Fig. S9a, the mineralization efficiency of Glu in the presence of Fe(III) and H_2O_2 is significantly higher than that observed when only Fe(III) is present, due to the presence of the photo-Fenton process. This finding is consistent with the degradation efficiency of Glu presented in Fig. 3a. Hence, these results illustrate that Glu was mineralized to form CO_2 and H_2O. Moreover, the TOC values obtained experimentally are higher than the values calculated from the concentration of Glu and carboxylic acid products, indicating the presence of other organic compounds in the system. Although these organic substances cannot be detected under our experimental conditions, they will enter the cloud water gas phase, further participating in atmospheric photochemical reactions and eventually being mineralized into H_2O and CO_2. In the presence of H_2O_2, as Glu undergoes photodegradation, the concentration of H_2O_2 in the system continues to decrease until it is completely consumed (Fig. S9b).

3.5 Insight into the mechanism of Glu transformation

The light-driven transformation mechanism of Glu in the presence of Fe(III) was investigated, with a focus on the $^{\bullet}OH$-mediated and the ligand-to-metal charge transfer (LMCT) process. The key difference between the two processes lies in the generation of glutamate radials: the $^{\bullet}OH$-mediated process involves a free radical mechanism initiated by hydrogen abstraction, whereas the LMCT pathway proceeds via an electron transfer process driven by photoexcitation. To provide a clear comparison, the two mechanisms are illustrated separately in Scheme 1 summarizing the possible Glu degradation pathway, derived from IC-MS analysis of the detected products.

In the $^{\bullet}OH$-mediated process, the α-carbon of Glu is identified as the primary site attacked for $^{\bullet}OH$ attack, initiating the transformation process. Hydrogen abstraction by $^{\bullet}OH$ results in the formation of glutamate alkyl radical ($R\text{-}C^{\bullet}(COO^-)NH_3^+$) and H_2O. Subsequently, this alkyl radical reacts with O_2 to generate the alkylperoxy radical ($ROO^{\bullet}$), which is further converted to alkoxy radical ($RO^{\bullet}$) (Goldman et al., 2021; von Sonntag and Schuchmann, 1991). The formation of $RO^{\bullet}$ is followed by a deamination process, which leads to the formation of ammonium (NH_4^+) and 2-oxoadipic acid through the cleavage of the amino group (Vel Leitner et al., 2002). Due to the presence of an oxo group (C=O) adjacent to a carboxyl group (COOH), 2-oxoadipic acid is chemically unstable and prone to self-decomposition via decarboxylation, resulting in the formation of succinic acid (Penteado et al., 2019). Further oxidation of succinic acid produces smaller carboxylic acids (Charbouillot et al., 2012).

In contrast, the LMCT process is initiated upon irradiation, resulting in the reduction of Fe(III) to Fe(II) and the generation of a radical centered on the oxygen atom of α-carboxyl group of glutamic acid ($R\text{-}CH(NH_3^+)C^+O^{\bullet}O^-$). This high reactive radical undergoes a decarboxylation process, resulting in the formation of an alkyl radical ($R\text{-}CH^{\bullet}NH_3^+$). Subsequently, the radical chain reaction propagates in the presence of O_2, leading to the formation of smaller carboxylic acids. It is critical to highlight that the only carboxylic acids detected under the same conditions are formic acid and acetic acid. This is different from the $^{\bullet}OH$-mediated process, in which succinate is first formed and then further decomposed into compounds such as other small molecular carboxylic acids.

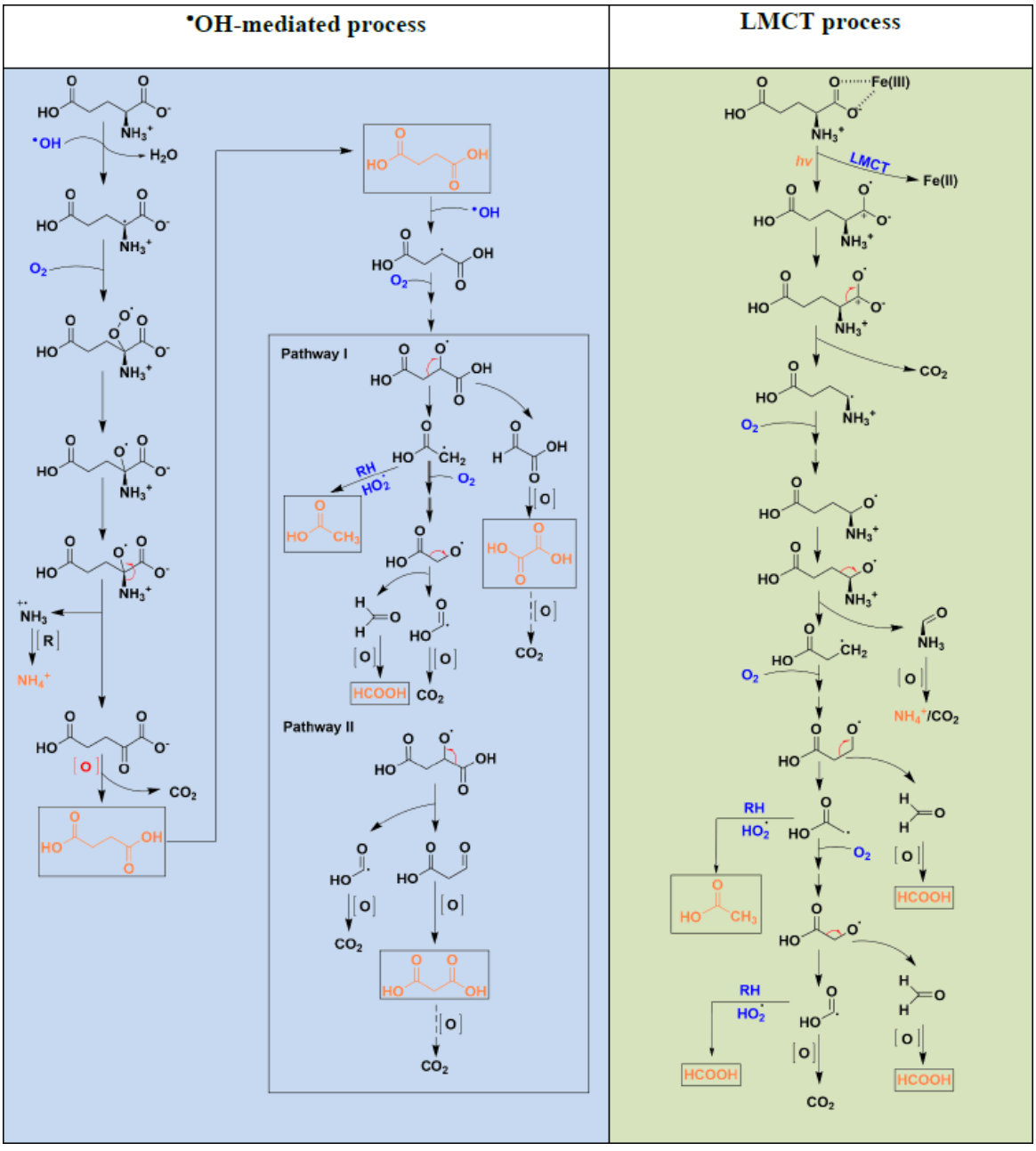

Scheme 1. The mechanism of Glu degradation in the presence of Fe(III) by the •OH attacking process and by the LMCT process. Products in orange are detected by IC-MS.

4 Atmospheric implications

This study systematically investigated the complexation of Glu with Fe(II)/Fe(III), its effect on the typical atmospheric reactions (Fenton reaction and Fe(III) photolysis), and its fate in the atmospheric aqueous phase. Our findings reveal that iron–amino acid (Fe-AA) complexes significantly modify the Fe(II)/Fe(III) cycle and •OH budget, diverging from the "classic" photo-Fenton mechanisms. Specifically, Fe(II)–Glu reacts with H_2O_2 at a rate constant 2 orders of magnitude higher than Fe(II) alone, potentially improving the iron cycle. Conversely, Fe(III)–Glu exhibits a lower quantum yield under irradiation, suppressing the Fe(III)/Fe(II) cycle. Moreover, both reactions result in lower •OH generation, as they favor the formation of Glu oxidation products (Glu_{ox}), thus partially affecting atmospheric oxidative capacity.

To date, the concentration of the Fe(II)/Fe(III)–Glu in cloud water has not yet been directly measured. Hence, based on the reported mean concentrations of Glu (87 nM) (Renard et al., 2022), Fe(II) (1 µM) (Deguillaume et al., 2014), and

Fe(III) (0.5 µM) (Deguillaume et al., 2014) in cloud water from the Puy de Dôme station (PUY – France), the fraction of Fe(II)–Glu and Fe(III)–Glu was calculated to be around 8.7×10^{-10}–2.1×10^{-4} % and 6.1×10^{-2}–2.4×10^{-1} % using Hyss software at a pH range of 3–7 respectively. Cloud water spans a wide pH range (3–7), which influences iron speciation and redox cycling. Low pH enhances iron solubility but may reduce Fe–Glu complexation by altering ligand binding. Nevertheless, in polluted regions with elevated iron and amino acid levels, the absolute Fe–Glu concentration may remain appreciable despite a lower complexation fraction. In contrast, marine clouds often contain lower concentrations of both Fe and amino acid (like Glu is around 33 pM collected in Venice on the Sacca San Biagio Island; Barbaro et al., 2011), leading to a smaller Fe–Glu fraction. Moreover, the concentration of Glu in cloud droplets may increase during the cloud water evaporation, leading to an increase in the concentration of iron–Glu complexes. This shift could alter atmospheric Fenton reaction dynamics, reducing $^{\bullet}$OH production, particularly at night (Galloway et al., 2014; Shulman et al., 1997). Similarly, the lower quantum yield of the Fe(III)–Glu under irradiation inhibits the Fe(II)/Fe(III) cycle and $^{\bullet}$OH generation, especially in daytime conditions. Likewise, the variations in light intensity due to diurnal cycles and cloud cover modulate the photolysis rates of iron–ligand complexes and the generation of reactive radicals. Taken together, these factors suggest that the photochemical processes involving Fe–Glu complexes are highly condition-dependent, leading to variable degradation and pathways of amino acids in atmospheric aqueous phases. This underscores the need to incorporate such environmental dependencies into atmospheric models.

In addition, recent studies reported that the average AAs contribution corresponded to 9.1 % of the dissolved organic carbon (DOC) (Bianco et al., 2016), highlighting their significance. Hence, Fe-AAs play a crucial role in iron speciation, stability, and $^{\bullet}$OH budget in atmospheric aqueous phases, which suggests that the inclusion of Fe-AAs in atmospheric aqueous-phase models is essential for accurately estimating $^{\bullet}$OH production, a key driver of atmospheric oxidation. Moreover, irradiation of Glu in the presence of Fe(III) demonstrated two different mechanisms ($^{\bullet}$OH mediated and LMCT process), leading to the generation of different products, which can further influence the atmospheric chemical composition, particularly through the formation of aqueous secondary organic aerosols (aqSOA) (Ervens et al., 2014). Overall, the observed generation of NH_4^+ during the Glu photo-degradation suggests a potential transformation pathway from organic nitrogen to inorganic nitrogen species in cloud water, providing a mechanistic link between organic nitrogen and ammonium. This finding is in line with previous reports (Mopper and Zika, 1987) that emphasize the role of amino acids in nitrogen cycling in the atmosphere. The generation of carboxylic acids further increases atmospheric complexity, as the generated carboxylic acids (e.g., oxalic acid) can complex iron and influence consequent photochemistry. In fact, atmospheric models often simplify the distribution and interactions of transition metal ions (TMIs) with organic compounds, including AAs. This study highlights the crucial role of the LMCT process in AA oxidation, which should be considered in atmospheric modeling as well.

Data availability. The data may be requested from the corresponding author.

Supplement. The supplement related to this article is available online at https://doi.org/10.5194/acp-25-12087-2025-supplement.

Author contributions. PC: investigation, formal analysis, and writing (original draft); GM: funding acquisition, writing (review and editing), and supervision; MS: writing (review and editing) and supervision; GV: technical support; DSF, TS, and HaH: writing (review and editing); MB: conceptualization, writing (review and editing), and supervision.

Competing interests. The contact author has declared that none of the authors has any competing interests.

Disclaimer. Publisher's note: Copernicus Publications remains neutral with regard to jurisdictional claims made in the text, published maps, institutional affiliations, or any other geographical representation in this paper. While Copernicus Publications makes every effort to include appropriate place names, the final responsibility lies with the authors.

Financial support. This work was supported by the Agence Nationale de la Recherche of France in the frame of the PRCI project REACTE.

Review statement. This paper was edited by Thomas Berkemeier and reviewed by two anonymous referees.

References

Alpert, P. A., Dou, J., Corral Arroyo, P., Schneider, F., Xto, J., Luo, B., Peter, T., Huthwelker, T., Borca, C. N., Henzler, K. D., Schaefer, T., Herrmann, H., Raabe, J., Watts, B., Krieger, U. K., and Ammann, M.: Photolytic radical persistence due to anoxia in viscous aerosol particles, Nat. Commun., 12, 1769, https://doi.org/10.1038/s41467-021-21913-x, 2021.

Angle, K. J., Neal, E. E., and Grassian, V. H.: Enhanced Rates of Transition-Metal-Ion-Catalyzed Oxidation of S(IV) in Aqueous Aerosols: Insights into Sulfate Aerosol Formation in the Atmosphere, Environ. Sci. Technol., 55, 10291–10299, https://doi.org/10.1021/acs.est.1c01932, 2021.

Bader, H., Sturzenegger, V., and Hoigné, J.: Photometric method for the determination of low concentrations of hydrogen peroxide by the peroxidase catalyzed oxidation of N,N-diethyl-*p*-phenylenediamine (DPD), Water Res., 22, 1109–1115, https://doi.org/10.1016/0043-1354(88)90005-X, 1988.

Barbaro, E., Zangrando, R., Moret, I., Barbante, C., Cescon, P., and Gambaro, A.: Free amino acids in atmospheric particulate matter of Venice, Italy, Atmos. Environ., 45, 5050–5057, https://doi.org/10.1016/j.atmosenv.2011.01.068, 2011.

Battaglia Jr., M. A., Weber, R. J., Nenes, A., and Hennigan, C. J.: Effects of water-soluble organic carbon on aerosol pH, Atmos. Chem. Phys., 19, 14607–14620, https://doi.org/10.5194/acp-19-14607-2019, 2019.

Bianco, A., Passananti, M., Perroux, H., Voyard, G., Mouchel-Vallon, C., Chaumerliac, N., Mailhot, G., Deguillaume, L., and Brigante, M.: A better understanding of hydroxyl radical photochemical sources in cloud waters collected at the puy de Dôme station – experimental versus modelled formation rates, Atmos. Chem. Phys., 15, 9191–9202, https://doi.org/10.5194/acp-15-9191-2015, 2015.

Bianco, A., Voyard, G., Deguillaume, L., Mailhot, G., and Brigante, M.: Improving the characterization of dissolved organic carbon in cloud water: Amino acids and their impact on the oxidant capacity, Sci. Rep., 6, 37420, https://doi.org/10.1038/srep37420, 2016.

Bianco, A., Vaïtilingom, M., Bridoux, M., Chaumerliac, N., Pichon, J.-M., Piro, J.-L., and Deguillaume, L.: Trace Metals in Cloud Water Sampled at the Puy De Dôme Station, Atmosphere, 8, 225, https://doi.org/10.3390/atmos8110225, 2017.

Bianco, A., Deguillaume, L., Vaïtilingom, M., Nicol, E., Baray, J.-L., Chaumerliac, N., and Bridoux, M.: Molecular Characterization of Cloud Water Samples Collected at the Puy de Dôme (France) by Fourier Transform Ion Cyclotron Resonance Mass Spectrometry, Environ. Sci. Technol., 52, 10275–10285, https://doi.org/10.1021/acs.est.8b01964, 2018.

Bianco, A., Passananti, M., Brigante, M., and Mailhot, G.: Photochemistry of the Cloud Aqueous Phase: A Review, Molecules, 25, 423, https://doi.org/10.3390/molecules25020423, 2020.

Bossmann, S. H., Oliveros, E., Göb, S., Siegwart, S., Dahlen, E. P., Payawan, L., Straub, M., Wörner, M., and Braun, A. M.: New Evidence against Hydroxyl Radicals as Reactive Intermediates in the Thermal and Photochemically Enhanced Fenton Reactions, J. Phys. Chem. A, 102, 5542–5550, https://doi.org/10.1021/jp980129j, 1998.

Buxton, G. V., Greenstock, C. L., Helman, W. P., and Ross, A. B.: Critical Review of rate constants for reactions of hydrated electrons, hydrogen atoms and hydroxyl radicals ($^{\bullet}OH/^{\bullet}O^{-}$ in Aqueous Solution, J. Phys. Chem. Ref. Data, 17, 513–886, https://doi.org/10.1063/1.555805, 1988.

Charbouillot, T., Gorini, S., Voyard, G., Parazols, M., Brigante, M., Deguillaume, L., Delort, A.-M., and Mailhot, G.: Mechanism of carboxylic acid photooxidation in atmospheric aqueous phase: Formation, fate and reactivity, Atmos. Environ., 56, 1–8, https://doi.org/10.1016/j.atmosenv.2012.03.079, 2012.

Christensen, H., Sehested, K., and Corfitzen, H.: Reactions of hydroxyl radicals with hydrogen peroxide at ambient and elevated temperatures, J. Phys. Chem., 86, 1588–1590, https://doi.org/10.1021/j100206a023, 1982.

Deguillaume, L., Charbouillot, T., Joly, M., Vaïtilingom, M., Parazols, M., Marinoni, A., Amato, P., Delort, A.-M., Vinatier, V., Flossmann, A., Chaumerliac, N., Pichon, J. M., Houdier, S., Laj, P., Sellegri, K., Colomb, A., Brigante, M., and Mailhot, G.: Classification of clouds sampled at the puy de Dôme (France) based on 10 yr of monitoring of their physicochemical properties, Atmos. Chem. Phys., 14, 1485–1506, https://doi.org/10.5194/acp-14-1485-2014, 2014.

Edwards, K. C., Klodt, A. L., Galeazzo, T., Schervish, M., Wei, J., Fang, T., Donahue, N. M., Aumont, B., Nizkorodov, S. A., and Shiraiwa, M.: Effects of Nitrogen Oxides on the Production of Reactive Oxygen Species and Environmentally Persistent Free Radicals from α-Pinene and Naphthalene Secondary Organic Aerosols, J. Phys. Chem. A, 126, 7361–7372, https://doi.org/10.1021/acs.jpca.2c05532, 2022.

Ervens, B., Sorooshian, A., Lim, Y. B., and Turpin, B. J.: Key parameters controlling OH-initiated formation of secondary organic aerosol in the aqueous phase (aqSOA), J. Geophys. Res.-Atmos., 119, 3997–4016, https://doi.org/10.1002/2013JD021021, 2014.

Gabet, A., Guy, C., Fazli, A., Métivier, H., de Brauer, C., Brigante, M., and Mailhot, G.: The ability of recycled magnetite nanoparticles to degrade carbamazepine in water through photo-Fenton oxidation at neutral pH, Sep. Purif. Technol., 317, 123877, https://doi.org/10.1016/j.seppur.2023.123877, 2023.

Galloway, M. M., Powelson, M. H., Sedehi, N., Wood, S. E., Millage, K. D., Kononenko, J. A., Rynaski, A. D., and De Haan, D. O.: Secondary Organic Aerosol Formation during Evaporation of Droplets Containing Atmospheric Aldehydes, Amines, and Ammonium Sulfate, Environ. Sci. Technol., 48, 14417–14425, https://doi.org/10.1021/es5044479, 2014.

Gligorovski, S., Strekowski, R., Barbati, S., and Vione, D.: Environmental Implications of Hydroxyl Radicals ((•)OH), Chem. Rev., 115, 13051–13092, https://doi.org/10.1021/cr500310b, 2015.

Goldman, M. J., Green, W. H., and Kroll, J. H.: Chemistry of Simple Organic Peroxy Radicals under Atmospheric through Combustion Conditions: Role of Temperature, Pressure, and NO_x Level, J. Phys. Chem. A, 125, 10303–10314, https://doi.org/10.1021/acs.jpca.1c07203, 2021.

Guo, J., Tilgner, A., Yeung, C., Wang, Z., Louie, P. K. K., Luk, C. W. Y., Xu, Z., Yuan, C., Gao, Y., Poon, S., Herrmann, H., Lee, S., Lam, K. S., and Wang, T.: Atmospheric Peroxides in a Polluted Subtropical Environment: Seasonal Variation, Sources and Sinks, and Importance of Heterogeneous Processes, Environ. Sci. Technol., 48, 1443–1450, https://doi.org/10.1021/es403229x, 2014.

Hoops, S., Sahle, S., Gauges, R., Lee, C., Pahle, J., Simus, N., Singhal, M., Xu, L., Mendes, P., and Kummer, U.: COPASI – a COmplex PAthway SImulator, Bioinformatics, 22, 3067–3074, https://doi.org/10.1093/bioinformatics/btl485, 2006.

Kanakidou, M., Myriokefalitakis, S., and Tsigaridis, K.: Aerosols in atmospheric chemistry and biogeochemical cycles of nutrients, Environ. Res. Lett., 13, 063004, https://doi.org/10.1088/1748-9326/aabcdb, 2018.

Kremer, M. L.: The Fenton Reaction. Dependence of the Rate on pH, J. Phys. Chem. A, 107, 1734–1741, https://doi.org/10.1021/jp020654p, 2003.

Long, Y., Charbouillot, T., Brigante, M., Mailhot, G., Delort, A.-M., Chaumerliac, N., and Deguillaume, L.: Evaluation

of modeled cloud chemistry mechanism against laboratory irradiation experiments: The H_xO_y/iron/carboxylic acid chemical system, Atmos. Environ., 77, 686–695, https://doi.org/10.1016/j.atmosenv.2013.05.037, 2013.

Mace, K. A., Kubilay, N., and Duce, R. A.: Organic nitrogen in rain and aerosol in the eastern Mediterranean atmosphere: An association with atmospheric dust, J. Geophys. Res.-Atmos., 108, https://doi.org/10.1029/2002JD002997, 2003.

Marion, A., Brigante, M., and Mailhot, G.: A new source of ammonia and carboxylic acids in cloud water: The first evidence of photochemical process involving an iron-amino acid complex, Atmos. Environ., 195, 179–186, https://doi.org/10.1016/j.atmosenv.2018.09.060, 2018.

Masuda, T., Nakano, S., and Kondo, M.: Rate constants for the reactions of OH radicals with the enzyme proteins as determined by the p-nitrosodimethylaniline method, J. Radiat. Res., 14, 339–345, https://doi.org/10.1269/jrr.14.339, 1973.

Matos, J. T. V., Duarte, R. M. B. O., and Duarte, A. C.: Challenges in the identification and characterization of free amino acids and proteinaceous compounds in atmospheric aerosols: A critical review, TrAC-Trend. Anal. Chem., 75, 97–107, https://doi.org/10.1016/j.trac.2015.08.004, 2016.

Mopper, K. and Zika, R. G.: Free amino acids in marine rains: evidence for oxidation and potential role in nitrogen cycling, Nature, 325, 246–249, https://doi.org/10.1038/325246a0, 1987.

Motohashi, N. and Saito, Y.: Competitive Measurement of Rate Constants for Hydroxyl Radical Reactions Using Radiolytic Hydroxylation of Benzoate, Chem. Pharm. Bull., 41, 1842–1845, https://doi.org/10.1248/cpb.41.1842, 1993.

Neyens, E. and Baeyens, J.: A review of classic Fenton's peroxidation as an advanced oxidation technique, J. Hazard. Mater., 98, 33–50, https://doi.org/10.1016/S0304-3894(02)00282-0, 2003.

Penteado, F., Lopes, E. F., Alves, D., Perin, G., Jacob, R. G., and Lenardão, E. J.: α-Keto Acids: Acylating Agents in Organic Synthesis, Chem. Rev., 119, 7113–7278, https://doi.org/10.1021/acs.chemrev.8b00782, 2019.

Pye, H. O. T., Nenes, A., Alexander, B., Ault, A. P., Barth, M. C., Clegg, S. L., Collett Jr., J. L., Fahey, K. M., Hennigan, C. J., Herrmann, H., Kanakidou, M., Kelly, J. T., Ku, I.-T., McNeill, V. F., Riemer, N., Schaefer, T., Shi, G., Tilgner, A., Walker, J. T., Wang, T., Weber, R., Xing, J., Zaveri, R. A., and Zuend, A.: The acidity of atmospheric particles and clouds, Atmos. Chem. Phys., 20, 4809–4888, https://doi.org/10.5194/acp-20-4809-2020, 2020.

Rachmilovich-Calis, S., Masarwa, A., Meyerstein, N., Meyerstein, D., and van Eldik, R.: New Mechanistic Aspects of the Fenton Reaction, Chem.-Eur. J., 15, 8303–8309, https://doi.org/10.1002/chem.200802572, 2009.

Renard, P., Brissy, M., Rossi, F., Leremboure, M., Jaber, S., Baray, J.-L., Bianco, A., Delort, A.-M., and Deguillaume, L.: Free amino acid quantification in cloud water at the Puy de Dôme station (France), Atmos. Chem. Phys., 22, 2467–2486, https://doi.org/10.5194/acp-22-2467-2022, 2022.

Samavat, S., Gholami, N., and Nazari, K.: Complexation of Iron (III) With Citrate and Tartarate Anions in Perturbed Aqueous Solutions Using Potentiometry and Difference UV/Vis and IR Spectrophotometric Methods, Acta Chim. Slov., 54, URN:NBN:SI:DOC-57Z7KIF4, 2007.

Samy, S., Robinson, J., and Hays, M. D.: An advanced LC-MS (Q-TOF) technique for the detection of amino acids in atmospheric aerosols, Anal. Bioanal. Chem., 401, 3103–3113, https://doi.org/10.1007/s00216-011-5238-2, 2011.

Scheres Firak, D., Schaefer, T., Senff, P., Cheng, P., Sarakha, M., Brigante, M., Mailhot, G., and Herrmann, H.: Fenton-like Reactions in Acidic Environments: New Mechanistic Insights and Implications to Atmospheric Particle-Phase Chemistry, ACS E&ST Air, https://doi.org/10.1021/acsestair.5c00077, 2025.

Shah, V., Jacob, D. J., Moch, J. M., Wang, X., and Zhai, S.: Global modeling of cloud water acidity, precipitation acidity, and acid inputs to ecosystems, Atmos. Chem. Phys., 20, 12223–12245, https://doi.org/10.5194/acp-20-12223-2020, 2020.

Shulman, M. L., Charlson, R. J., and James Davis, E.: The effects of atmospheric organics on aqueous droplet evaporation, J. Aerosol Sci., 28, 737–752, https://doi.org/10.1016/S0021-8502(96)00469-7, 1997.

Soriano-Molina, P., García Sánchez, J. L., Alfano, O. M., Conte, L. O., Malato, S., and Sánchez Pérez, J. A.: Mechanistic modeling of solar photo-Fenton process with Fe^{3+}-EDDS at neutral pH, Appl. Catal. B-Environ., 233, 234–242, https://doi.org/10.1016/j.apcatb.2018.04.005, 2018.

Sorooshian, A., Wang, Z., Coggon, M. M., Jonsson, H. H., and Ervens, B.: Observations of Sharp Oxalate Reductions in Stratocumulus Clouds at Variable Altitudes: Organic Acid and Metal Measurements During the 2011 E-PEACE Campaign, Environ. Sci. Technol., 47, 7747–7756, https://doi.org/10.1021/es4012383, 2013.

Strathmann, T. J. and Stone, A. T.: Reduction of Oxamyl and Related Pesticides by FeII: Influence of Organic Ligands and Natural Organic Matter, Environ. Sci. Technol., 36, 5172–5183, https://doi.org/10.1021/es0205939, 2002.

Sun, L., Wu, C.-H., and Faust, B. C.: Photochemical Redox Reactions of Inner-Sphere Copper(II)-Dicarboxylate Complexes: Effects of the Dicarboxylate Ligand Structure on Copper(I) Quantum Yields, J. Phys. Chem. A, 102, 8664–8672, https://doi.org/10.1021/jp982045g, 1998.

Tilgner, A., Bräuer, P., Wolke, R., and Herrmann, H.: Modelling multiphase chemistry in deliquescent aerosols and clouds using CAPRAM3.0i, J. Atmos. Chem., 70, 221–256, https://doi.org/10.1007/s10874-013-9267-4, 2013.

Triesch, N., van Pinxteren, M., Salter, M., Stolle, C., Pereira, R., Zieger, P., and Herrmann, H.: Sea Spray Aerosol Chamber Study on Selective Transfer and Enrichment of Free and Combined Amino Acids, ACS Earth Space Chem., 5, 1564–1574, https://doi.org/10.1021/acsearthspacechem.1c00080, 2021.

van Pinxteren, M., Müller, C., Iinuma, Y., Stolle, C., and Herrmann, H.: Chemical Characterization of Dissolved Organic Compounds from Coastal Sea Surface Microlayers (Baltic Sea, Germany), Environ. Sci. Technol., 46, 10455–10462, https://doi.org/10.1021/es204492b, 2012.

van Pinxteren, M., Zeppenfeld, S., Fomba, K. W., Triesch, N., Frka, S., and Herrmann, H.: Amino acids, carbohydrates, and lipids in the tropical oligotrophic Atlantic Ocean: sea-to-air transfer and atmospheric in situ formation, Atmos. Chem. Phys., 23, 6571–6590, https://doi.org/10.5194/acp-23-6571-2023, 2023.

Vel Leitner, N. K., Berger, P., and Legube, B.: Oxidation of Amino Groups by Hydroxyl Radicals in Relation to the Oxidation Degree of the α-Carbon, Environ. Sci. Technol., 36, 3083–3089, https://doi.org/10.1021/es0101173, 2002.

von Sonntag, C. and Schuchmann, H.-P.: The Elucidation of Peroxyl Radical Reactions in Aqueous Solution with the Help of Radiation-Chemical Methods, Angew. Chem. Int. Edit., 30, 1229–1253, https://doi.org/10.1002/anie.199112291, 1991.

Wang, T. L., Tong, H. W., Yan, X. Y., Sheng, L. Q., Yang, J., and Liu, S. M.: Determination of Volatile Carbonyl Compounds in Cigarette Smoke by LC-DAD, Chromatographia, 62, 631–636, https://doi.org/10.1365/s10337-005-0675-8, 2005.

Wang, Z., Chen, X., Ji, H., Ma, W., Chen, C., and Zhao, J.: Photochemical Cycling of Iron Mediated by Dicarboxylates: Special Effect of Malonate, Environ. Sci. Technol., 44, 263–268, https://doi.org/10.1021/es901956x, 2010.

Weller, C., Horn, S., and Herrmann, H.: Photolysis of Fe(III) carboxylato complexes: Fe(II) quantum yields and reaction mechanisms, J. Photoch. Photobio. A, 268, 24–36, https://doi.org/10.1016/j.jphotochem.2013.06.022, 2013.

Yuan, Y., Feng, L., Xie, N., Zhang, L., and Gong, J.: Rapid photochemical decomposition of perfluorooctanoic acid mediated by a comprehensive effect of nitrogen dioxide radicals and Fe^{3+}/Fe^{2+} redox cycle, J. Hazard. Mater., 388, 121730, https://doi.org/10.1016/j.jhazmat.2019.121730, 2020.